Phase-field description of brittle fracture in plates and shells

Josef Kiendl[a,*], Marreddy Ambati[a], Laura De Lorenzis[a], Hector Gomez[b], Alessandro Reali[c,d]

[a]*Institute of Applied Mechanics – TU Braunschweig, Bienroder Weg 87, 38106 Braunschweig, Germany.*
[b]*Departamento de Métodos Matemáticos, Universidade da Coruña, Campus de A Coruña, 15071, A Coruña, Spain.*
[c]*Dipartimento di Ingegneria Civile ed Architettura, Università degli Studi di Pavia, Via Ferrata 3, 27100 Pavia, Italy.*
[d]*Technische Universität München – Institute for Advanced Study, Lichtenbergstraße 2a, 85748 Garching, Germany.*

Abstract

We present an approach for phase-field modeling of fracture in thin structures like plates and shells, where the kinematics are defined by midsurface variables. Accordingly, the phase field is defined as a two-dimensional field on the midsurface of the structure. In this work, we consider brittle fracture with a split of the elastic energy into tensile and compressive terms and a Kirchhoff-Love shell model for structural analysis. We show that for a correct description of fracture, the variation of strains through the shell thickness has to be considered and the split into tensile and compressive elastic energy has to be computed at various points through the thickness. This prohibits the typical separation of the elastic energy into membrane and bending terms. Instead, the energy is split into tension and compression terms, each depending on both membrane and bending deformations. For numerical analysis, we employ isogeometric discretizations and a rotation-free Kirchhoff-Love shell formulation. In several numerical examples we show the applicability of the approach and detailed comparisons with 3D solid simulations confirm its accuracy and efficiency.

Keywords: Phase field; Fracture; Shell; Plate; Kirchhoff-Love; Isogeometric analysis

1. Introduction

The prediction of fracture in thin structures is a crucial aspect for the safety assessment of engineering structures in various industries, e.g., in the automotive (car bodies), aeronautic (aircraft fuselages), and marine (ship hulls, tanks, and vessels) industries, or renewable energies (wind turbines). A special challenge in such applications is the correct combination of fracture models, which are mostly derived in a solid mechanics framework, with structural models like plates and shells, which have a special load-carrying behavior and are based on dimensionally-reduced kinematics.

*Corresponding author
Email address: j.kiendl@tu-braunschweig.de (Josef Kiendl)

Numerical models for fracture mechanics can be divided into two main categories, namely discrete and smeared approaches. In the discrete approaches, cracks are modeled as discontinuities, either between elements, e.g., through the so-called cohesive zone modeling approach, or within elements by enriching the displacement field using the partition of unity method. A particular form of this approach is the extended finite element method (XFEM), which has also been applied to shells and plates in several works [1–4]. The main drawbacks of discrete approaches are the need for ad hoc criteria for crack nucleation and propagation as well as the difficulty to model complex fracture patterns like crack branching and merging. An interesting alternative can be found in the phase-field approach to fracture. Here, the discrete crack is approximated by a crack phase field, or simply phase field, which smoothens the discontinuity over a small region. This approach can describe crack initiation and propagation as well as crack branching and merging without ad hoc criteria and with no need for crack tracking techniques. Phase-field models for brittle fracture are mostly derived from the work of Bourdin et al. [5, 6] who regularized the variational form of Griffith's theory presented by Francfort and Marigo [7]. Over the last years, this approach has gained a lot of interest with applications to both static and dynamic brittle fracture [8–13], and it has also been extended to ductile fracture [14–21]. However, there have been only few approaches combining phase-field modeling of fracture with structural models such as plates and shells. Ulmer et. al [22] presented an approach for brittle fracture in thin plates and shells, where shells are considered as a combination of a plate and a standard membrane. Accordingly, the elastic energy is divided into bending and membrane contributions. The membrane part is additively decomposed into tensile and compressive terms, while no split on the bending term is performed, such that the tensile membrane energy and the full bending energy contribute to crack evolution and are degraded in the fracture zone. Amiri et al. [23] also modeled fracture in thin shells with the phase-field approach, however, without any split in tension and compression terms, making the model limited to applications with pure tension states of stress. More recently, Areias et al. [24] presented an approach for finite-strain plates and shells, where they assume two independent phase fields, corresponding to the lower and upper face of the shell, in order to correctly account for the fracture behavior in bending. Ambati et al. [25] have applied phase-field modeling of fracture in a solid-shell approach, where no shell-specific considerations for fracture are needed, but volumetric discretization and analysis of both the shell structure and the phase field are necessary.

Isogeometric analysis (IGA) was introduced by Hughes et al. [26] as a new paradigm to bridge the gap between computer-aided design (CAD) and analysis, by adopting Non-Uniform Rational B-Splines (NURBS), which are used for geometry representation in CAD, as basis functions for analysis. In the past ten years, IGA has gained enormous interest in nearly all fields of computational mechanics and, in particular, it has led to many new developments in shell analysis. The smoothness of the basis functions allows for efficient implementations of rotation-free Kirchhoff-

Love shell models [27–33], but there are also several developments in the context of Reissner-Mindlin shells [34–37] and solid-shells [38–42], as well as novel approaches such as blended shells [43], hierarchic shells [44], and rotation-free shear deformable shells [45]. Furthermore, IGA was applied successfully to phase-field modeling of fracture. Borden et al. [46] exploited the higher continuity of isogeometric basis functions for proposing a higher-order phase-field model, which was combined by Hesch et al. [47] with hierarchical refinement. Schillinger et al. [48] proposed isogeometric collocation methods for phase-field modeling of fracture, and Ambati et al. [25] employed isogeometric discretizations for fracture in solid-shells.

In this paper, we pursue an approach for phase-field modeling of fracture in plates and shells, where the structure is described by a surface model and fracture is described by a single phase field. We briefly review the existing approaches [22, 23] and make some observations, which, in our opinion, do not permit a correct description of fracture in pure bending or combined bending and membrane stress states. Based on these observations, we propose a new approach which leads to a correct description of the mechanical response in such situations. A key aspect is that fracture is driven by the tensile part of the total strains, which are composed by membrane and bending contributions and vary through the shell thickness. For numerical analysis we employ isogeometric discretizations for both the structure and the phase field. We use a Kirchhoff-Love shell formulation [27], however, the proposed approach is general and can be applied to other shell and plate formulations as well. We test our approach on several numerical examples representing different strain states for shell and plate structures. In all examples, we perform detailed comparisons to results obtained with three-dimensional solid simulations, which confirm the accuracy of the proposed approach.

2. Formulation

We first give a brief review of the employed phase-field model of brittle fracture in a solid mechanics setting, and then show how this can be projected consistently to dimensionally reduced continua such as plates and shells.

2.1. Phase-field model of brittle fracture with tension-compression split

The model is based on the variational formulation of brittle fracture by Francfort and Marigo [7], where the entire process of crack initiation, propagation and branching is governed by the minimization problem of the free energy functional

$$E(\boldsymbol{\varepsilon}, \Gamma) = \int_{\Omega} \psi_e(\boldsymbol{\varepsilon}) d\Omega + G_c \int_{\Gamma} d\Gamma, \tag{1}$$

where $\psi_e(\boldsymbol{\varepsilon})$ is the elastic strain energy density, $\boldsymbol{\varepsilon}$ the strain tensor, and G_c the material fracture toughness. Ω represents the problem domain and $\Gamma \subset \Omega$ is an internal discontinuity boundary, i.e., the set of crack surfaces. Assuming isotropic linear elasticity, the strain energy density is given by

$$\psi_e(\boldsymbol{\varepsilon}) = \frac{1}{2}\lambda\,(\mathrm{tr}(\boldsymbol{\varepsilon}))^2 + \mu\,\mathrm{tr}(\boldsymbol{\varepsilon}^2), \tag{2}$$

with λ and μ as the Lamé constants. In the regularized formulation proposed by Bourdin et al. [5] the fracture energy is approximated by

$$\int_\Gamma G_c\,d\Gamma \approx \int_\Omega G_c \left(\frac{1}{4\ell_0}(1-s)^2 + \ell_0|\nabla s|^2\right) d\Omega = \int_\Omega \psi_s(s, \nabla s) d\Omega. \tag{3}$$

The phase-field variable s takes on values between 1, corresponding to intact material, and 0, corresponding to fully cracked material. The length parameter $\ell_0 > 0$ controls the width of the transition zone from cracked to uncracked material. If ℓ_0 tends towards zero, the phase-field approximation converges to Griffith's linear elastic fracture mechanics solution, featuring a discrete fracture surface, in the Γ-convergence sense [6].

For a realistic modeling of fracture, where material cracks in tension but not in compression, the strain tensor is additively decomposed in tensile and compressive contributions, $\boldsymbol{\varepsilon}^+$ and $\boldsymbol{\varepsilon}^-$, respectively

$$\boldsymbol{\varepsilon} = \boldsymbol{\varepsilon}^+ + \boldsymbol{\varepsilon}^-. \tag{4}$$

Following Miehe et al. [10], this split is obtained through a spectral decomposition of the strain tensor

$$\boldsymbol{\varepsilon} = \sum_{i=1}^{3} \varepsilon_i\, \boldsymbol{n}_i \otimes \boldsymbol{n}_i, \tag{5}$$

where ε_i and $\boldsymbol{n}_i$ are the eigenvalues and eigenvectors of $\boldsymbol{\varepsilon}$, i.e., the principal strains and principal directions, respectively. $\boldsymbol{\varepsilon}^+$ and $\boldsymbol{\varepsilon}^-$ are then defined through the positive and negative principal strains

$$\boldsymbol{\varepsilon}^\pm = \sum_{i=1}^{3} \langle \varepsilon_i \rangle^\pm \boldsymbol{n}_i \otimes \boldsymbol{n}_i, \tag{6}$$

with $\langle x \rangle^\pm = (x \pm |x|)/2$.

With this split of the strain tensor, we obtain the split of the strain energy density and stress

tensor into tensile and compressive terms as follows

$$\psi_e^{\pm} = \frac{1}{2}\lambda \left(\langle \mathrm{tr}(\boldsymbol{\varepsilon})\rangle^{\pm}\right)^2 + \mu \,\mathrm{tr}\left((\boldsymbol{\varepsilon}^{\pm})^2\right), \tag{7}$$

$$\boldsymbol{\sigma}^{\pm} = \lambda \langle \mathrm{tr}(\boldsymbol{\varepsilon})\rangle^{\pm} \boldsymbol{I} + 2\mu\, \boldsymbol{\varepsilon}^{\pm}, \tag{8}$$

with $\boldsymbol{I}$ being the identity tensor. In the cracking zone, the tensile terms are degraded through a degradation function $g(s)$ and we obtain

$$\psi_e(\boldsymbol{\varepsilon}, s) = g(s)\, \psi_e^{+}(\boldsymbol{\varepsilon}) + \psi_e^{-}(\boldsymbol{\varepsilon}), \tag{9}$$

$$\boldsymbol{\sigma}(\boldsymbol{\varepsilon}, s) = g(s)\, \boldsymbol{\sigma}^{+}(\boldsymbol{\varepsilon}) + \boldsymbol{\sigma}^{-}(\boldsymbol{\varepsilon}), \tag{10}$$

where we adopt the degradation function proposed by [10]

$$g(s) = (1-\eta)\, s^2 + \eta, \tag{11}$$

with $\eta << 1$ as a residual stiffness factor, added for avoiding ill-posedness in the fully cracked state. Finally, the regularized energy functional is given by

$$E_{\ell_0}(\boldsymbol{\varepsilon}, s) = \int_{\Omega} \left(g(s)\, \psi_e^{+}(\boldsymbol{\varepsilon}) + \psi_e^{-}(\boldsymbol{\varepsilon}) + \psi_s(s, \nabla s)\right) d\Omega, \tag{12}$$

and we can derive the strong form of the governing equations as

$$\mathrm{div}\ \boldsymbol{\sigma} = \boldsymbol{0}, \tag{13}$$

$$\left(\frac{4\,\ell_0(1-\eta)\psi_e^{+}}{G_c} + 1\right) s - 4\,\ell_0^2 \Delta s = 1. \tag{14}$$

In order to ensure irreversibility of the crack evolution, a history variable representing the maximum positive elastic strain energy density obtained up to a time (or pseudo-time) instant t is introduced [10]

$$\mathcal{H}(t) := \max_{\tau \in [0,t]} \psi_e^{+}(\tau). \tag{15}$$

This history variable then substitutes ψ_e^{+} in the strong form equation (14)

$$\left(\frac{4\,\ell_0(1-\eta)\mathcal{H}}{G_c} + 1\right) s - 4\,\ell_0^2 \Delta s = 1. \tag{16}$$

Such approaches, which use a split of the strain tensor in order to avoid material cracking in compression, are often referred to as anisotropic fracture models. Accordingly, we speak of an isotropic fracture model if the entire strain energy is degraded, corresponding to a material behavior

that fractures equally in tension and compression. This distinction is a key aspect in the approaches for shells and plates discussed in the following section.

2.2. Phase-field modeling of fracture for plates and shells

In dimensionally reduced structural models, such as shells and plates, the 3D continuum is usually described by its midsurface and a thickness h. Deformation is typically described in terms of (pseudo-)strain variables like membrane strains, curvature changes, and possibly transverse shear strains, which are all assumed to be constant through the thickness. The crucial question is then how a fracture model like the one shown above can be described consistently in terms of such kinematic variables. In the following exposition, we consider a Kirchhoff-Love shell model, which means that transverse shear strains are neglected, including Kirchhoff plates as a special case. However, the proposed approach could be applied analogously to shear deformable Reissner-Mindlin plates and shells.

2.2.1. Shell kinematics

We first briefly introduce the shell kinematics and then show how it can be linked to the phase-field approach to fracture presented above. For the shell governing equations, a curvilinear coordinate system is used with θ^1, θ^2 as the natural coordinates of the midsurface, and θ^3 as the thickness coordinate, with $-h/2 \leq \theta^3 \leq h/2$. Index notation is used where it is more convenient, with Greek indices taking on values $\{1, 2\}$ and with implied summation over repeated indices.

A point on the shell midsurface is described by $\mathbf{r}$, and the covariant tangent base vectors are obtained as $\mathbf{a}_\alpha = \mathbf{r}_{,\alpha}$, with $(\cdot)_{,\alpha} = \partial(\cdot)/\partial\theta^\alpha$. Contravariant base vectors $\mathbf{a}^\alpha$ are defined by $\mathbf{a}^\alpha \cdot \mathbf{a}_\beta = \delta^\alpha_\beta$, with δ^α_β as the Kronecker delta, and we further define a unit normal vector by

$$\mathbf{a}_3 = \frac{\mathbf{a}_1 \times \mathbf{a}_2}{|\mathbf{a}_1 \times \mathbf{a}_2|} \,. \tag{17}$$

With the tangent and normal vectors we can compute the first and second fundamental forms of the surface as

$$a_{\alpha\beta} = \mathbf{a}_\alpha \cdot \mathbf{a}_\beta \,, \tag{18}$$

$$b_{\alpha\beta} = \mathbf{a}_{\alpha,\beta} \cdot \mathbf{a}_3 \,, \tag{19}$$

where $a_{\alpha\beta}$ are known as the metric coefficients and $b_{\alpha\beta}$ as the curvature coefficients of the midsurface.

For computing strain variables, we distinguish between the deformed and undeformed configurations, where all variables related to the undeformed configuration are indicated by $\mathring{(\cdot)}$. With the metric and curvature coefficients of the deformed and undeformed configurations, we obtain

membrane strains $\boldsymbol{\varepsilon}^m = \varepsilon^m_{\alpha\beta}\, \mathring{\mathbf{a}}^\alpha \otimes \mathring{\mathbf{a}}^\beta$ and curvature changes $\boldsymbol{\kappa} = \kappa_{\alpha\beta}\, \mathring{\mathbf{a}}^\alpha \otimes \mathring{\mathbf{a}}^\beta$ with

$$\varepsilon^m_{\alpha\beta} = \frac{1}{2}(a_{\alpha\beta} - \mathring{a}_{\alpha\beta})\,, \tag{20}$$

$$\kappa_{\alpha\beta} = \mathring{b}_{\alpha\beta} - b_{\alpha\beta}\,. \tag{21}$$

The membrane strains describe the in-plane or membrane deformation of the midsurface, while the

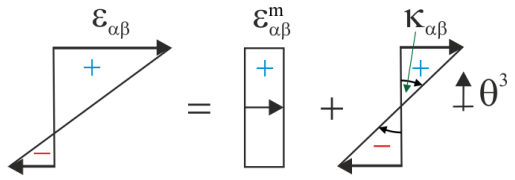

Figure 1: Separation of in-plane strains into membrane and bending contributions.

curvature changes describe the deformation due to bending. We note that (20)-(21) are naturally nonlinear strain measures accounting for large deformations. In this paper, we restrict ourselves to small deformation problems and use linearized versions of (20)-(21), which are presented in detail in Appendix A. It is crucial to note that both $\boldsymbol{\varepsilon}^m$ and $\boldsymbol{\kappa}$ induce the same type of strain components, and the total strain $\boldsymbol{\varepsilon}$ at any point in the shell is given by

$$\boldsymbol{\varepsilon}(\theta^3) = \boldsymbol{\varepsilon}^m + \theta^3 \boldsymbol{\kappa}\,. \tag{22}$$

Figure 1 illustrates equation (22), showing that the split into membrane and bending strains simply represents a split of $\boldsymbol{\varepsilon}(\theta^3)$ into a constant and a symmetrically linear part. Although it is common in shell analysis to keep this split also for stress and energy expressions, we will show that this is not appropriate in the context of fracture.

Since the shell model is based on the plane stress assumption, the stress tensor and strain energy density are given by

$$\boldsymbol{\sigma} = \lambda\, \mathrm{tr}(\boldsymbol{\varepsilon})\, \boldsymbol{I} + 2\mu\, \boldsymbol{\varepsilon} - \frac{\lambda^2}{2\,(\lambda + 2\,\mu)}\, \mathrm{tr}(\boldsymbol{\varepsilon})\, \boldsymbol{I}, \tag{23}$$

$$\psi_e = \frac{1}{2}\lambda\, (\mathrm{tr}(\boldsymbol{\varepsilon}))^2 + \mu\, \mathrm{tr}(\boldsymbol{\varepsilon}^2) - \frac{\lambda^2}{2\,(\lambda + 2\,\mu)}\, (\mathrm{tr}(\boldsymbol{\varepsilon}))^2, \tag{24}$$

where $\boldsymbol{\varepsilon}$ is the 2D tensor given by (22) and the λ^2-terms represent the plane stress condition $\varepsilon_{33} = 0$.

Expressed in terms of the shell kinematic variables, (23)-(24) read as

$$\boldsymbol{\sigma}(\theta^3) = \lambda \operatorname{tr}(\boldsymbol{\varepsilon}^m + \theta^3 \boldsymbol{\kappa})\, \boldsymbol{I} + 2\mu \left(\boldsymbol{\varepsilon}^m + \theta^3 \boldsymbol{\kappa}\right) - \frac{\lambda^2}{2\,(\lambda + 2\,\mu)} \operatorname{tr}(\boldsymbol{\varepsilon}^m + \theta^3 \boldsymbol{\kappa})\, \boldsymbol{I}, \tag{25}$$

$$\psi_e(\theta^3) = \frac{1}{2}\lambda \left(\operatorname{tr}\left(\boldsymbol{\varepsilon}^m + \theta^3 \boldsymbol{\kappa}\right)\right)^2 + \mu \operatorname{tr}\left(\left(\boldsymbol{\varepsilon}^m + \theta^3 \boldsymbol{\kappa}\right)^2\right) - \frac{\lambda^2}{2\,(\lambda + 2\,\mu)} \left(\operatorname{tr}\left(\boldsymbol{\varepsilon}^m + \theta^3 \boldsymbol{\kappa}\right)\right)^2. \tag{26}$$

Note that (25)-(26) describe the stresses and strains energy density at arbitrary points in the three-dimensional shell continuum. The stresses are typically integrated through the thickness, yielding membrane forces $\boldsymbol{n}$ and bending moments $\boldsymbol{m}$ as stress resultants

$$\boldsymbol{n} = \int_{-h/2}^{h/2} \boldsymbol{\sigma}\, d\theta^3, \tag{27}$$

$$\boldsymbol{m} = \int_{-h/2}^{h/2} \boldsymbol{\sigma}\, \theta^3 d\theta^3. \tag{28}$$

In a standard linear elastic model, this integration can be performed analytically and the stress resultants are obtained as

$$\boldsymbol{n} = h\left(\lambda \operatorname{tr}(\boldsymbol{\varepsilon}^m)\, \boldsymbol{I} + 2\mu\, \boldsymbol{\varepsilon}^m - \frac{\lambda^2}{2\,(\lambda + 2\,\mu)} \operatorname{tr}(\boldsymbol{\varepsilon}^m)\, \boldsymbol{I}\right), \tag{29}$$

$$\boldsymbol{m} = \frac{h^3}{12}\left(\lambda \operatorname{tr}(\boldsymbol{\kappa})\, \boldsymbol{I} + 2\mu\, \boldsymbol{\kappa} - \frac{\lambda^2}{2\,(\lambda + 2\,\mu)} \operatorname{tr}(\boldsymbol{\kappa})\, \boldsymbol{I}\right). \tag{30}$$

We furthermore introduce the strain energy surface density Ψ_e, describing the strain energy per unit area of the midsurface, as

$$\Psi_e = \int_{-h/2}^{h/2} \psi_e(\theta^3) d\theta^3. \tag{31}$$

Assuming linear elasticity, the integral (31) could also be computed analytically and might be separated into membrane and bending terms $\Psi_e = \Psi_e^m(\boldsymbol{\varepsilon}^m) + \Psi_e^b(\boldsymbol{\kappa})$ with

$$\Psi_e^m = h\left(\frac{1}{2}\lambda \left(\operatorname{tr}(\boldsymbol{\varepsilon}^m)\right)^2 + \mu \operatorname{tr}((\boldsymbol{\varepsilon}^m)^2) - \frac{\lambda^2}{2\,(\lambda + 2\,\mu)} \left(\operatorname{tr}(\boldsymbol{\varepsilon}^m)\right)^2\right), \tag{32}$$

$$\Psi_e^b = \frac{h^3}{12}\left(\frac{1}{2}\lambda \left(\operatorname{tr}(\boldsymbol{\kappa})\right)^2 + \mu \operatorname{tr}(\boldsymbol{\kappa}^2) - \frac{\lambda^2}{2\,(\lambda + 2\,\mu)} \left(\operatorname{tr}(\boldsymbol{\kappa})\right)^2\right). \tag{33}$$

It is also worth noting that (33) represents the strain energy surface density of a Kirchhoff plate.

2.2.2. *Previous approaches*

Approaches to combine shell models with a phase-field description of fracture using a single phase field were presented so far in [22, 23]. In the following, we briefly review these approaches and make some observations, which motivate the new approach proposed in the next section.

In [23], the full strain energy density (31) is degraded by the phase field, i.e., fracture will appear equally in tension and compression, which apparently does not correctly describe the nature of fracture. In the context of curved shells it is also worth noting that even under purely tensile loading compressive strains typically appear as a consequence of bending.

In [22], some split into tension and compression is performed. The elastic energy is first separated into membrane and bending terms as shown in (32)-(33), where the membrane part Ψ_e^m is split into Ψ_e^{m+} and Ψ_e^{m-} by a spectral decomposition of $\boldsymbol{\varepsilon}^m$, while no split is performed on the bending energy Ψ_e^b. For the modeling of fracture, the tensile membrane energy and the full bending energy are degraded, $\Psi_e = g(s)(\Psi_e^{m+} + \Psi_e^b) + \Psi_e^{m-}$. In our opinion, this approach has two significant shortcomings, which we briefly discuss in the following. The first problem lies in the separation of the elastic energy in membrane and bending terms, which also implies a separation of the strains into membrane and bending strains. Such an approach neglects the fact that $\boldsymbol{\varepsilon}^m$ and $\boldsymbol{\kappa}$ contribute to the same total strain $\boldsymbol{\varepsilon}$, see Equation (22) and Figure 1. This can lead to severe problems especially in cases of combined bending and compression. In such cases, the compressive membrane strains actually reduce the tensile strains induced by bending, reducing therefore the tendency of the material to crack. In Figure 2, we sketch a case of combined bending and compression where the

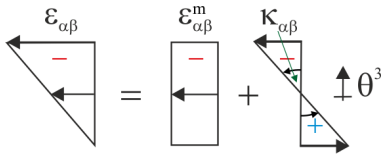

Figure 2: Combined bending and compression. Strain distribution over the thickness.

total strains are compressive everywhere. The separation of the strain energy into membrane and bending contributions, however, does not take this effect into account and might lead to fracture although the strains are purely compressive. The second problem of this approach is in the fact that the bending energy is degraded entirely without any split into tension and compression terms. Considering a case of pure bending (typically a plate), such an approach needs to be considered as an isotropic fracture model. Inspired by these two findings, we propose a new approach in the following.

2.3. Proposed approach

In this section, we present an approach for phase-field modeling of fracture for plates and shells with a focus on the correct modeling of the tension-compression split under bending and on the interaction of membrane and bending strains. For a correct prediction of fracture, we consider the total strain (22) and split it into tension and compression. Here it is important to note that the spectral decomposition of $\boldsymbol{\varepsilon}$ cannot be obtained by spectral decompositions of $\boldsymbol{\varepsilon}^m$ and $\boldsymbol{\kappa}$

$$\boldsymbol{\varepsilon}^{\pm}(\theta^3) = \left(\boldsymbol{\varepsilon}^m + \theta^3\boldsymbol{\kappa}\right)^{\pm} \neq \boldsymbol{\varepsilon}^{m\,\pm} + \theta^3\boldsymbol{\kappa}^{\pm}. \tag{34}$$

As a consequence, we cannot consider a split into tensile and compressive terms and into membrane and bending terms at the same time. It is also worth noting that splitting $\boldsymbol{\kappa}$ into positive and negative terms would have no physical meaning in the sense of a tension-compression split, since both positive and negative $\kappa_{\alpha\beta}$ induce tension as well as compression. Accordingly, we split the stress tensor and strain energy density into tensile and compressive terms based on the split of the total strain including both membrane and bending contributions

$$\boldsymbol{\sigma}^{\pm}(\theta^3) = \lambda\langle \mathrm{tr}(\boldsymbol{\varepsilon}^m + \theta^3\boldsymbol{\kappa})\rangle^{\pm}\,\boldsymbol{I} + 2\mu\,\left(\boldsymbol{\varepsilon}^m + \theta^3\boldsymbol{\kappa}\right)^{\pm} - \frac{\lambda^2}{2\,(\lambda+2\,\mu)}\,\langle \mathrm{tr}(\boldsymbol{\varepsilon}^m + \theta^3\boldsymbol{\kappa})\rangle^{\pm}\,\boldsymbol{I}, \tag{35}$$

$$\psi_e^{\pm}(\theta^3) = \frac{1}{2}\lambda\,\left(\langle \mathrm{tr}\left(\boldsymbol{\varepsilon}^m + \theta^3\boldsymbol{\kappa}\right)\rangle^{\pm}\right)^2 + \mu\,\mathrm{tr}\left(\left(\left(\boldsymbol{\varepsilon}^m + \theta^3\boldsymbol{\kappa}\right)^{\pm}\right)^2\right) - \frac{\lambda^2}{2\,(\lambda+2\,\mu)}\,\left(\langle \mathrm{tr}\left(\boldsymbol{\varepsilon}^m + \theta^3\boldsymbol{\kappa}\right)\rangle^{\pm}\right)^2. \tag{36}$$

The effective stress resultants are obtained by integrating (35) through the thickness and degrading the tensile stresses

$$\boldsymbol{n}(\boldsymbol{\varepsilon}^m, \boldsymbol{\kappa}, s) = \int_{-h/2}^{h/2} \left(g(s)\,\boldsymbol{\sigma}^{+}(\boldsymbol{\varepsilon}^m, \boldsymbol{\kappa}) + \boldsymbol{\sigma}^{-}(\boldsymbol{\varepsilon}^m, \boldsymbol{\kappa})\right) d\theta^3, \tag{37}$$

$$\boldsymbol{m}(\boldsymbol{\varepsilon}^m, \boldsymbol{\kappa}, s) = \int_{-h/2}^{h/2} \left(g(s)\,\boldsymbol{\sigma}^{+}(\boldsymbol{\varepsilon}^m, \boldsymbol{\kappa}) + \boldsymbol{\sigma}^{-}(\boldsymbol{\varepsilon}^m, \boldsymbol{\kappa})\right)\,\theta^3 d\theta^3. \tag{38}$$

Clearly, the decomposition and split operations in (35) depend on the thickness coordinate θ^3 leading to a nonlinear distribution of $\boldsymbol{\sigma}^{\pm}$ in thickness direction. Accordingly, the integrals in (37)-(38) cannot be obtained analytically. Instead, numerical integration is used, where in each integration point the total strain is computed as sum of membrane and bending contributions (22) and then $\boldsymbol{\varepsilon}^{\pm}$ and $\boldsymbol{\sigma}^{\pm}$ are computed as in a standard 2D plane stress problem, independently of the specific shell formulation. A remarkable advantage of this approach is that we can describe a varying degradation of stresses through the thickness although the phase field s, and with it the degradation function $g(s)$, are assumed as constant over the thickness. This allows for a very good approximation of the three-dimensional fracture problem with shell models and a single two-dimensional phase field, as will be also demonstrated in the numerical tests section.

For the energy functional, we also split the strain energy surface density (31) in tension and compression terms by integrating (36) through the thickness

$$\Psi_e^{\pm} = \int_{-h/2}^{h/2} \psi_e^{\pm}(\theta^3) d\theta^3. \tag{39}$$

With (39), the regularized energy functional of the shell can be written as

$$E_{\ell_0}(\boldsymbol{\varepsilon}^m, \boldsymbol{\kappa}, s) = \int_A \left(g(s)\, \Psi_e^+(\boldsymbol{\varepsilon}^m, \boldsymbol{\kappa}) + \Psi_e^-(\boldsymbol{\varepsilon}^m, \boldsymbol{\kappa}) + \Psi_s(s, \nabla s) \right) dA, \tag{40}$$

where A denotes the midsurface and Ψ_s is obtained by integrating ψ_s through the thickness

$$\Psi_s(s, \nabla s) = \int_{-h/2}^{h/2} \psi_s(s, \nabla s) d\theta^3 = h\, G_c \left(\frac{1}{4\ell_0}(1-s)^2 + \ell_0 |\nabla s|^2 \right). \tag{41}$$

2.4. Variational formulation and implementation

For the solution of the coupled problem, we employ a staggered approach [10, 13], where in each step, we first solve the momentum equation and then the phase-field equation. The weak form of the phase-field equation is

$$\int_A \left(\frac{4\,\ell_0(1-\eta)\mathcal{H}}{h\, G_c} + 1 \right) s\, \tilde{s}\, dA + 4\,\ell_0^2 \int_A \nabla s \cdot \nabla \tilde{s} dA = \int_A \tilde{s}\, dA. \tag{42}$$

where A indicates the shell midsurface and $\tilde{s}$ is a test function. Here, the history variable is defined as the maximum of the positive strain energy surface density (39)

$$\mathcal{H}(t) := \max_{\tau \in [0,t]} \Psi_e^+(\tau). \tag{43}$$

The weak form of the momentum equation is given by the virtual work expression of a Kirchhoff-Love shell

$$\int_A (\tilde{\boldsymbol{\varepsilon}} : \boldsymbol{n} + \tilde{\boldsymbol{\kappa}} : \boldsymbol{m})\, dA = \int_A \tilde{\boldsymbol{u}} \cdot \boldsymbol{f}\, dA, \tag{44}$$

where $\boldsymbol{f}$ is the external load, $\tilde{\boldsymbol{u}}$ is the test function, interpreted as virtual displacement, and $\tilde{\boldsymbol{\varepsilon}}, \tilde{\boldsymbol{\kappa}}$ are the corresponding virtual strain variables. For details on the linearization and discretization of (44), yielding the stiffness matrix and residual vector, we refer to [27, 31]. Due to the second derivatives inherent in the curvatures, C^1-continuity of the basis function is required. We employ NURBS-based isogeometric analysis, which provides the necessary continuity and allows for a rotation-free shell formulation [27], and, in the sense of an isoparametric approach, we use the same discretization also for the phase field. Integration through the thickness for computing the

stress resultants (37)-(38), as well as Ψ_e^+ (39), is performed numerically, where the strains at integration points outside the midsurface are obtained by the midsurface variables through Equation (22). It is worth noting that the numerical thickness integration does not imply discretization in thickness direction, and no additional evaluation of shape functions is necessary.

3. Numerical tests

In this section we test the proposed formulation on various numerical examples. In order to carefully investigate the different possible strain states in a shell, we first study some in-plane loading problem, then a series of plate problems, and finally curved shell problems. A focus in all the tests is to show that the shell fracture model appropriately approximates the 3D fracture model. For this purpose we perform all tests also with 3D computations, where we use isogeometric solid elements. We note that we have performed these computations also with solid-shell elements [25], in order to avoid possible locking effects, but due to the fine meshes employed there is practically no difference between the solid and solid-shell results. In all tests, quadratic NURBS are used (both for shells and solids) and for the integration through the shell thickness, we use three Gauss points, such that it is comparable to the solid computations.

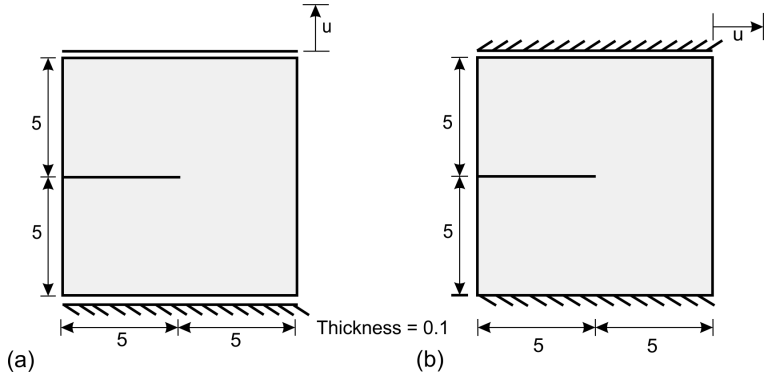

Figure 3: Single-edge notched (a) tension test and (b) shear test. Geometry and boundary conditions, dimensions in mm.

3.1. Single-edge notched specimen tension and shear test

We start with an example in a purely membrane state of stress, which is a well studied problem in the phase-field literature, see e.g. [5, 10, 11, 13, 25]. It consists of a square plate containing a straight horizontal notch, located at mid-height of the left edge. The geometric properties and boundary conditions of the specimen are shown in Figure 3. A vertical/horizontal displacement is applied to all points of the top edge for the tensile/shear test case. The material parameters are chosen as $E = 10 \times 10^8$ N/mm^2, $\nu = 0.3$, $G_c = 2$ N/mm and $\ell_0 = 0.05$ mm. For both tests, the

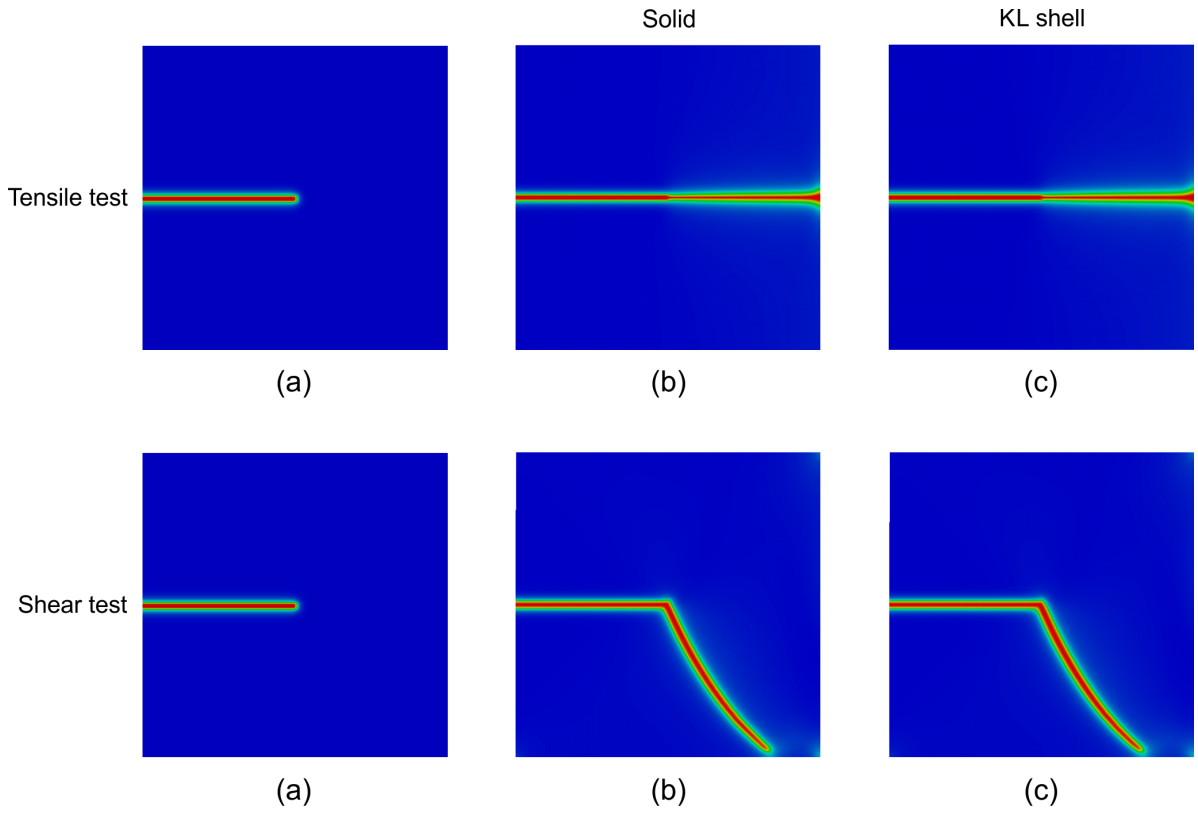

Figure 4: Single-edge notched specimen tension/shear test. (a-b) Crack phase field at initial and completely fractured states. (b-c) Comparison between results obtained with Kirchhoff-Love (KL) shell and solid elements.

spatial discretization contains $15,000$ elements and is refined a priori in the region where crack propagation is expected. The simulations are performed under displacement control with fixed displacement increments. Figure 4 shows the phase field at two instants, before crack initiation and after complete fracture for both the shell and the solid computations, with the colors indicating the value of the phase field ranging between 1 (blue) and 0 (red). The resulting crack paths coincide with those obtained in previous investigations [10, 11, 13, 25]. The corresponding load-displacement curves in Figure 5 confirm also quantitatively the very good agreement of the shell results with those obtained by 3D simulations.

3.2. Simply supported beam

In the following, we study a series of plate problems, starting with a rectangular plate simply supported on the two short sides and subjected to a constant load, see Figure 6. The material parameters are as follows: $E = 10 \times 10^9$ N/mm^2, $\nu = 0$, $G_c = 3$ N/mm, and $\ell_0 = 0.01$mm. Due to the setup and $\nu = 0$, this example represents a simple beam problem where the solution is constant in the width direction. The spatial discretization of the model comprises 7395 elements, with refinement in the central region where the crack is expected to form. The simulation is performed with

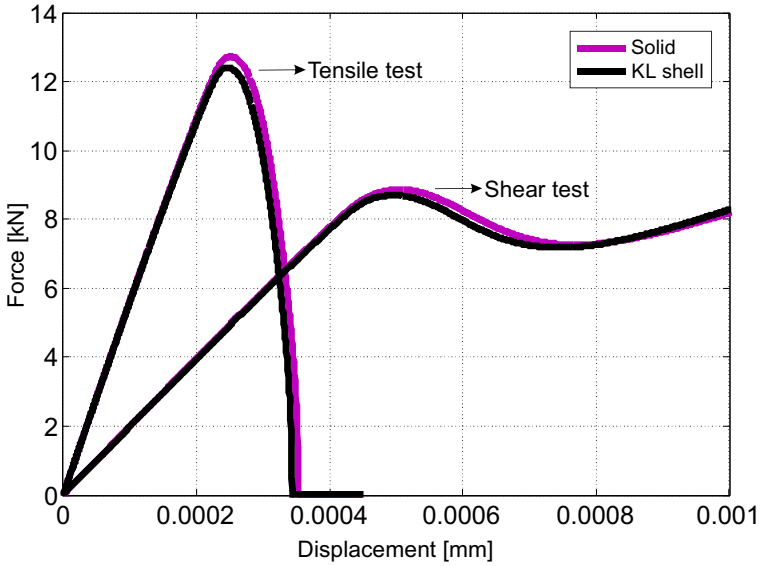

Figure 5: Single-edge notched specimen tension/shear test. Load-displacement curves. Comparison between KL shell and solid elements.

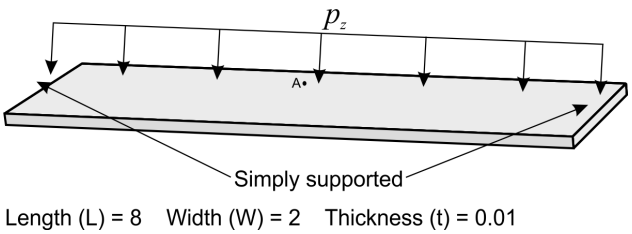

Figure 6: Simply supported beam modeled as a plate, with transverse loading. Problem setup, dimensions in mm.

arc-length control until failure and the transverse displacement u_z of a point (A) located at the center of the beam is monitored at every load step. Figure 7 illustrates the transverse deflection field and the phase field, on the undeformed and deformed configurations, at the final loading stage. A very good agreement of the shell and solid results can be observed. In order to demonstrate the importance of considering the split into tensile and compressive strains even in the case of pure bending, we also perform the shell computations with the approach from [22], i.e., degrading the full bending energy, see 2.2.2. As discussed above, we believe that such an approach corresponds to an isotropic fracture model. Accordingly, we will indicate the corresponding results as "isotropic KL plate model" (plate instead of shell because this investigation refers to pure bending). Although the results obtained with such a model look qualitatively very similar to the ones obtained with the proposed approach, large quantitative differences can be observed when looking at the force-displacement curves, see Figure 8. For the sake of comparison we also perform 3D solid computations with the isotropic fracture model which confirm the previously made interpre-

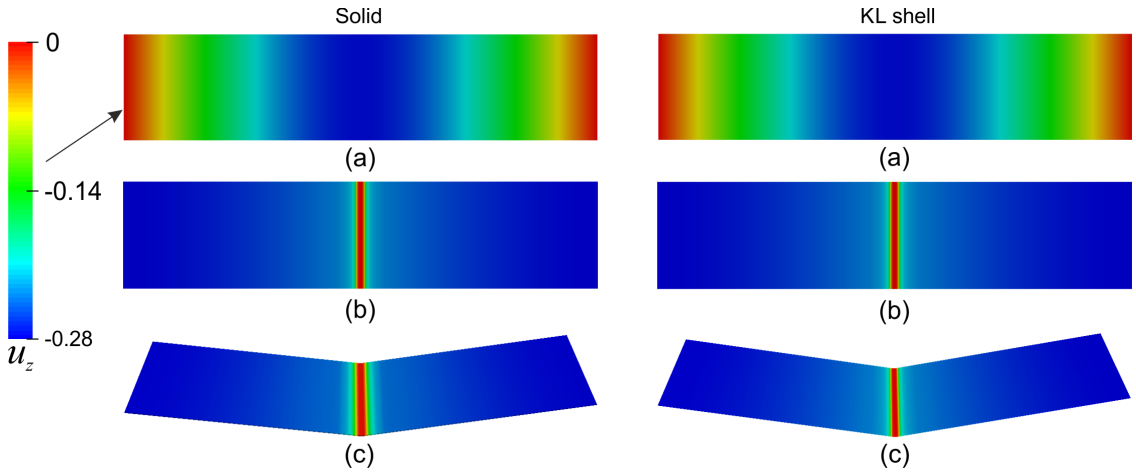

Figure 7: Simply supported beam with transverse loading. (a) Transverse deflection field and (b)-(c) crack phase field at final fracture stage, on the undeformed and the deformed configurations. Comparison between shell and solid solutions.

tation. As can be seen in the resulting load-displacement curves, the isotropic approaches lead to a significant underestimation of the critical load for a plate in bending. In order to confirm that this phenomenon is not limited to this simple example, we will perform this comparison in all the pure bending examples in the following.

In a next step, we use this simple example to demonstrate another crucial aspect, namely the importance of considering the additive nature of membrane and bending strains (22) when performing the split into tensile and compressive strains. For this purpose we add a compressive in-plane load, which is chosen such that the total strains are compressive everywhere, see Figure 9. This approach of "prestressing" for reducing tensile stresses is typically applied in the design of concrete structures. We perform the calculation both with our proposed formulation as well as with a shell formulation where tension and bending energy are degraded separately [22]. As can be seen in Figure 10, the separation into bending and membrane energy, indicated by "KL shell Ψ_e^m, Ψ_e^b", leads to fracture although the total strain is compressive everywhere. Indeed, the results are the same as in the case without compression, cf. Figure 8. With the approach proposed in this paper, instead, the interaction of bending and compression is correctly taken into account and no fracture appears. Furthermore, the results are in perfect agreement with those obtained by 3D elements.

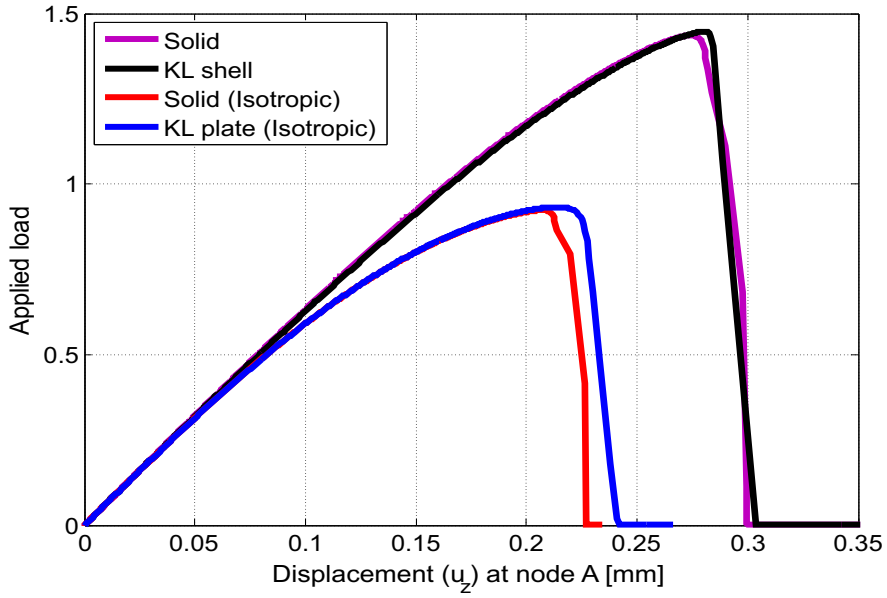

Figure 8: Simply supported beam with transverse loading. Load-displacement curves.

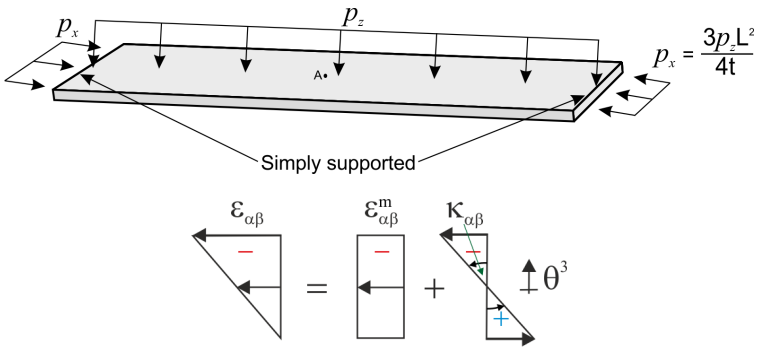

Figure 9: Simply supported beam, with transverse loading and compression. Problem setup (dimensions are the same as in Figure 6) and strain distribution over the thickness.

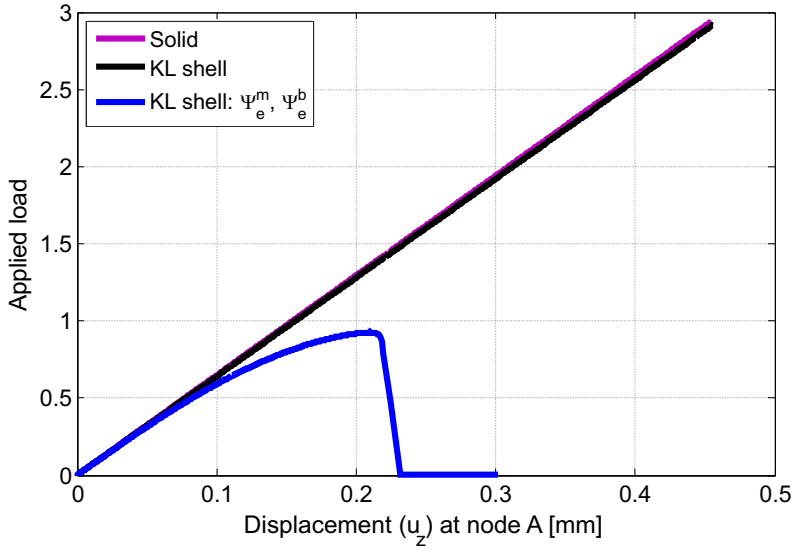

Figure 10: Simply supported beam with transverse loading and compression. Load-displacement curves.

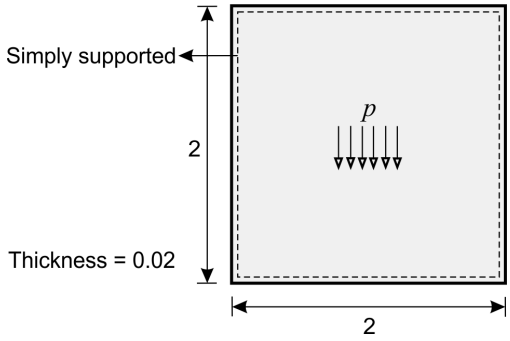

Figure 11: Simply supported plate. Geometry and boundary conditions, dimensions in mm.

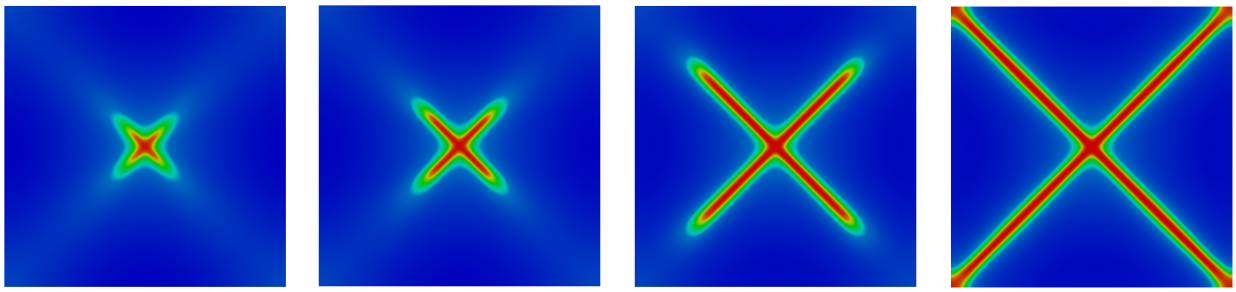

Figure 12: Simply supported plate. Crack phase field at various fracture stages.

3.3. Simply supported plate

While the previous example represented a state of unidirectional bending, i.e., a beam-like behavior, we now consider a plate with bidirectional bending. A square plate under uniform pressure loading is simply supported on all sides. For such a setup, previous investigations showed that four cracks initiate near the center and propagate towards the corners [49, 50]. The geometry and boundary conditions of the problem are illustrated in Figure 11 and the material parameters are $E = 190 \times 10^3$ N/mm^2, $\nu = 0.29$, $G_c = 0.295$ N/mm and $\ell_0 = 0.02$mm. Exploiting symmetry, only one quarter of the plate is modeled and discretized uniformly with 7225 elements and arc-length control is adopted. Figure 12 depicts the crack phase field obtained with the proposed formulation, at various stages. As can be seen, the crack initiates in the middle of the specimen and propagates towards the corners of the plate. Failure occurs once the boundaries of the specimen are reached. The results are in good agreement with the observations in [49, 50]. For plotting the load-displacement curves, we monitor the norm of the total displacement vector, defined as $u_{\text{norm}} = \sqrt{\frac{\hat{\boldsymbol{u}}^{\mathrm{T}}\,\hat{\boldsymbol{u}}}{n_{\text{cp}}}}$, where $\hat{\boldsymbol{u}}$ is the vector of the control point displacements and n_{cp} is the total number of control points. The results are depicted in Figure 13, where we can see again a good agreement

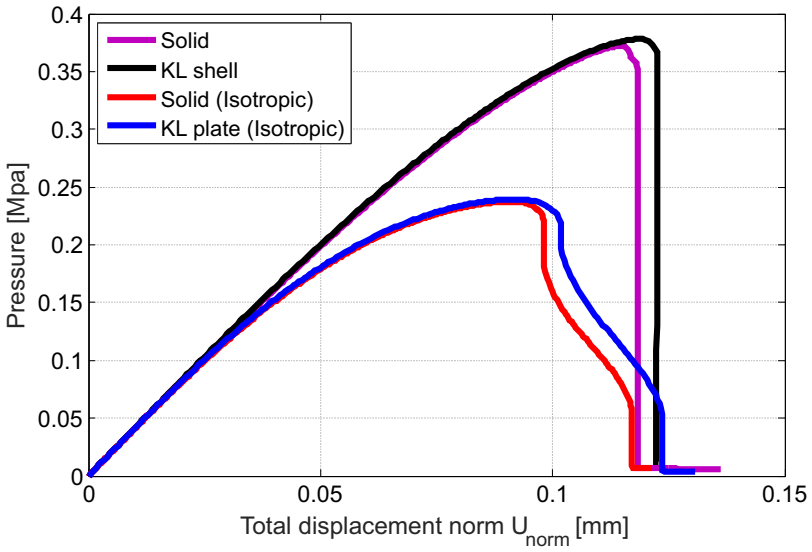

Figure 13: Simply supported plate. Load-displacement curves.

of the proposed model with the 3D solution as well as the confirmation regarding the isotropic models.

3.4. Annular plate

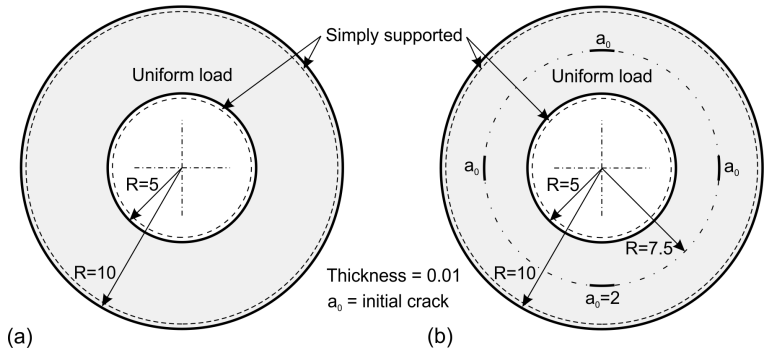

Figure 14: Annular plate. Geometry and boundary conditions (a) without initial cracks [51] and (b) with initial cracks [25]. Dimensions in mm.

We now model an annular plate simply supported at the inner and outer edges, with a uniformly distributed transverse load. This example has also been studied in [22, 25, 51]. We consider two cases: an initially uncracked plate, and a plate with four small initial cracks. The goal of the latter case is to investigate the capability of the phase-field formulation to deal with crack interaction and merging. Geometry and boundary conditions are depicted in Figure 14. The material parameters are $E = 10.92 \times 10^7$ N/mm^2, $\nu = 0$, $G_c = 3$ N/mm and $\ell_0 = 0.01$ mm. A discretization with 8,670 elements is used for the initially uncracked plate, whereas the plate with initial cracks consists of 7,395 elements. In both cases, local mesh refinement is used in the expected crack propagation region. Exploiting symmetry, only one quarter of the geometry is modeled. The simulation is performed under arc-length control. For the annular plate without initial cracks, Figure 15 shows the transverse deflection field and the phase field at the final loading stage. For the annular plate with initial cracks, the evolving crack path is illustrated in Figure 16, which proves the ability of the phase-field approach to naturally describe the interaction and merging of different cracks without the need for specific modeling features. Both problem cases have been computed with both shells and solids in anisotropic fracture as well as with their isotropic counterparts and the results are reported in Figures 17. As in the previous examples, the results confirm the validity of the proposed approach as well as the significant difference between isotropic and anisotropic fracture models in pure bending situations.

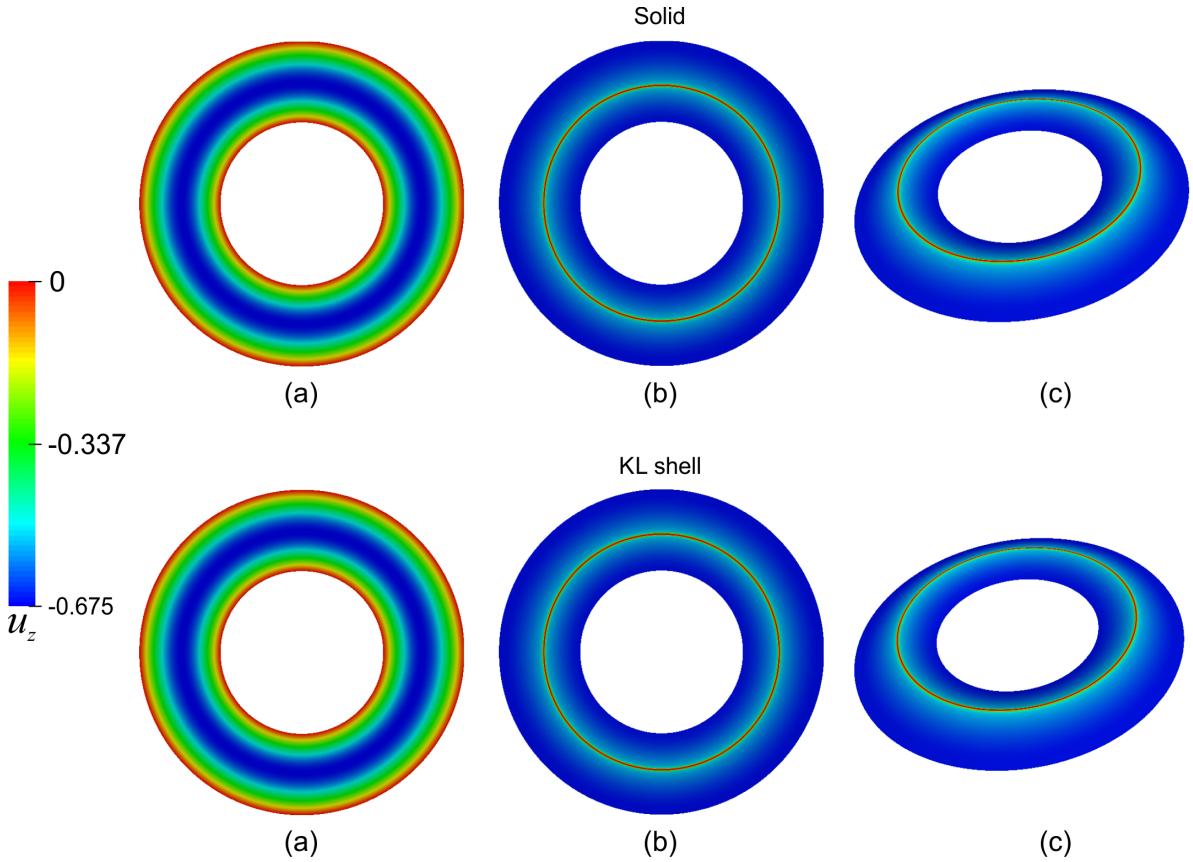

Figure 15: Annular plate without initial cracks. (a) Transverse deflection field and (b-c) crack phase field at final fracture stage, on the undeformed and the deformed configuration. Comparison between KL shell and solid elements.

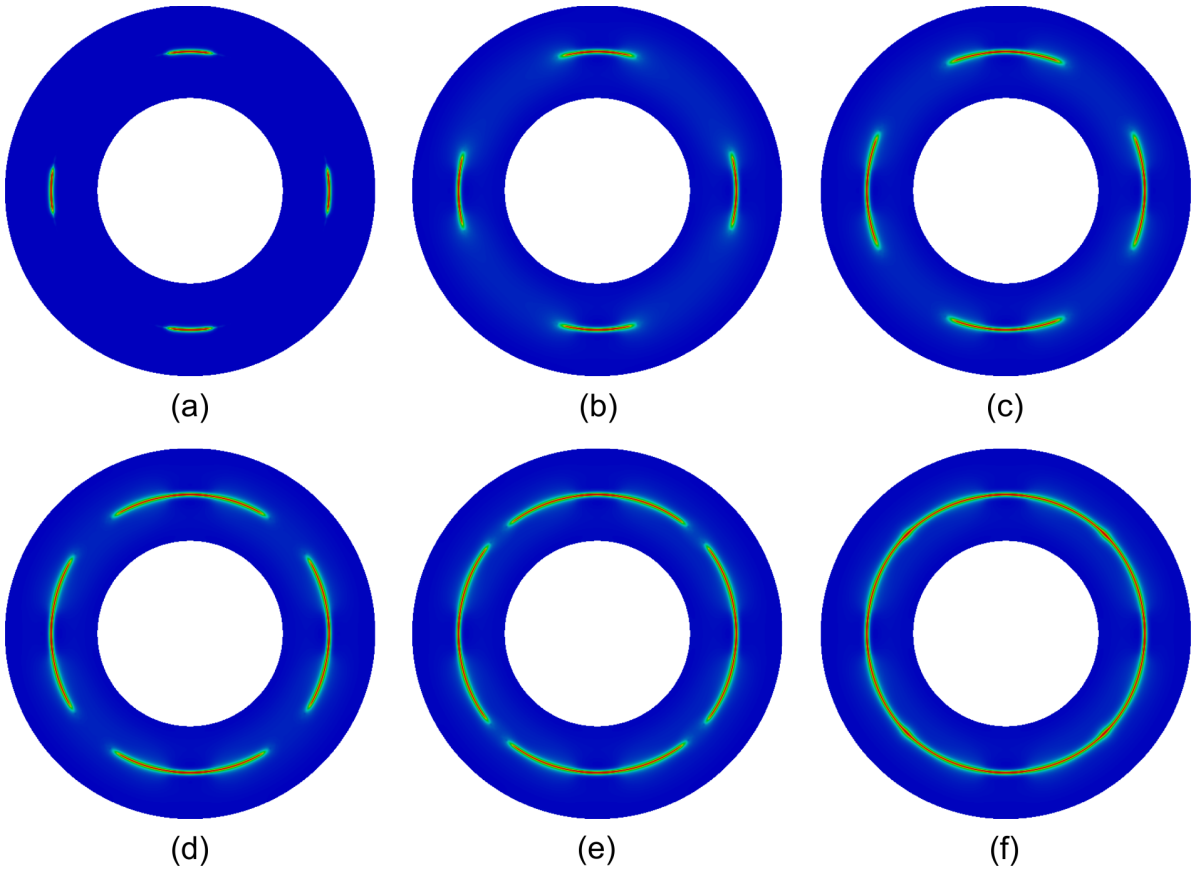

Figure 16: Annular plate with initial cracks. (a) Initial crack phase field and (b)-(f) crack phase field at various fracture stages.

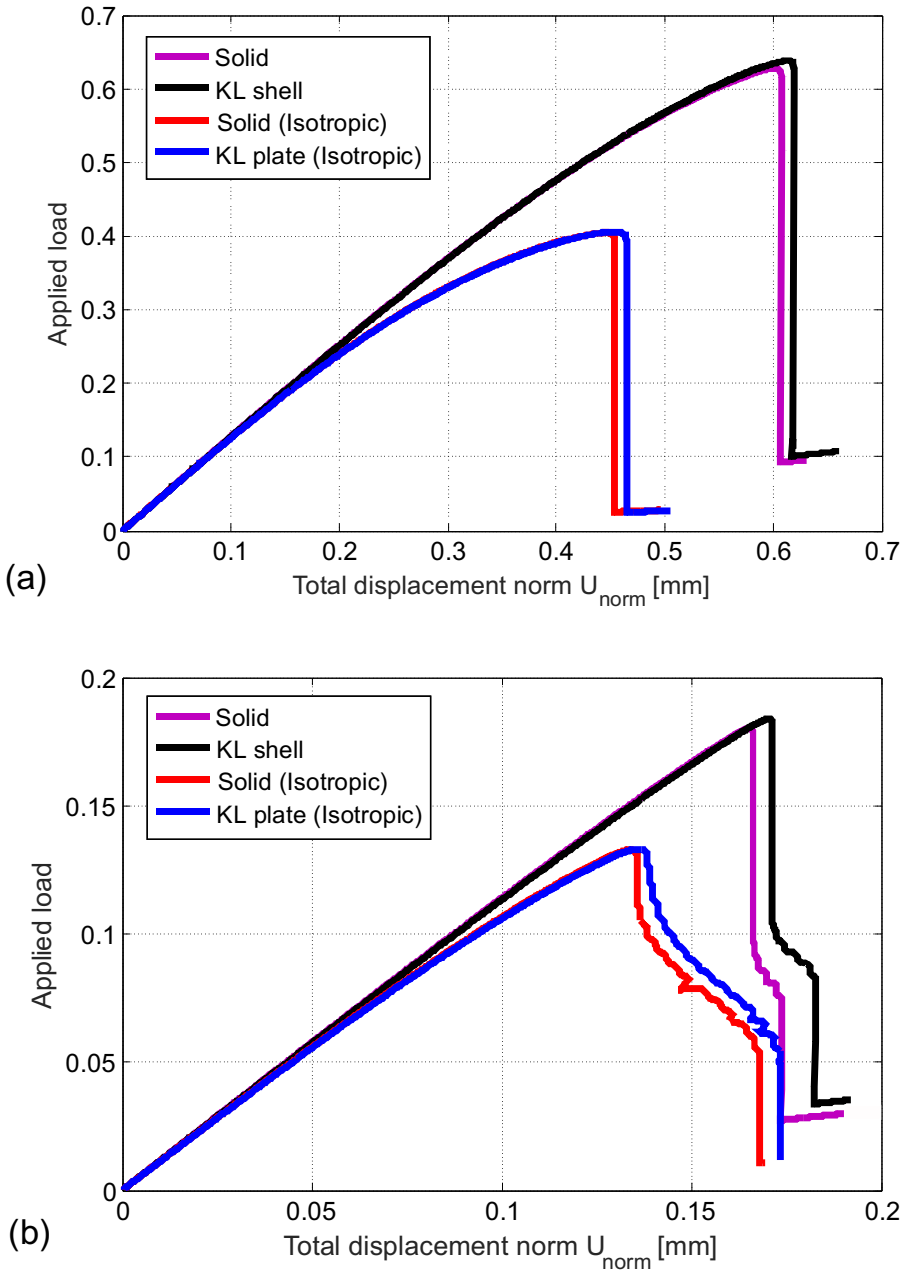

Figure 17: Annular plate. Load-displacement curves, (a) without initial cracks and (b) with initial cracks.

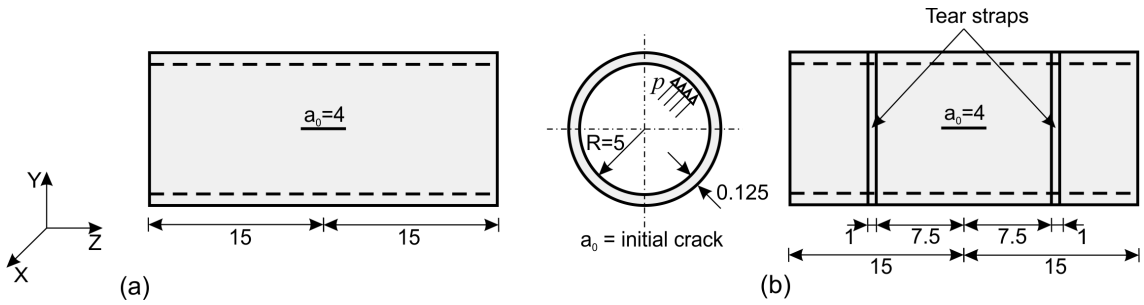

Figure 18: Notched cylinders under internal pressure (a) without tear straps, (b) with tear straps. Problem setup, dimensions in mm.

3.5. Notched cylinder under internal pressure

In the following, we study a couple of shell examples with combined bending and membrane action. The first example is an axially-notched cylindrical shell subjected to internal pressure, which has been studied also in [25]. As shown in Figure 18, we consider two cases, one without and one with the presence of tear straps. The aim of the latter is to restrain the axially propagating crack by inducing the so-called flapping, i.e., crack turning in the vicinity of the straps. The simulation setup is given in Figure 18. The displacements in X and Y directions are fixed at the cylinder ends. The material parameters taken from [25] are as follows: $E = 70 \times 10^3$ N/mm^2, $\nu = 0.3$, $G_c = 1.5$ N/mm and $\ell_0 = 0.05$ mm. The cylinder without tear straps is meshed with 20,800 elements, whereas the structure with straps is discretized with 20,580 elements. In both cases, local refinement is performed in the region where the crack is expected to form. Exploiting symmetry, only a quarter of the geometry is modeled. For the cylinder without tear straps, a series of snapshots with the crack phase field plotted on the deformed shape is shown in Figure 19. For visualization purposes, the elements with $s < 0.05$ are removed from the contour plots. A straight crack path is observed as expected. For the cylinder with tear straps, the deformed shape with the phase field contour plot is shown in Figure 20. It can be seen that the crack initially forms at the existing notch and then propagates parallel to the axis of the cylinder toward its ends. As the crack approaches the straps, a sudden redirection of its trajectory takes place with simultaneous branching in the circumferential direction. This phenomenon, termed flapping [52, 53], is successfully simulated by the proposed model. The corresponding load-displacement curves are given in Figure 21, which shows good agreement of the proposed formulation with the 3D simulation also in cases of combined membrane and bending action as well as in complex crack situations involving branching and flapping.

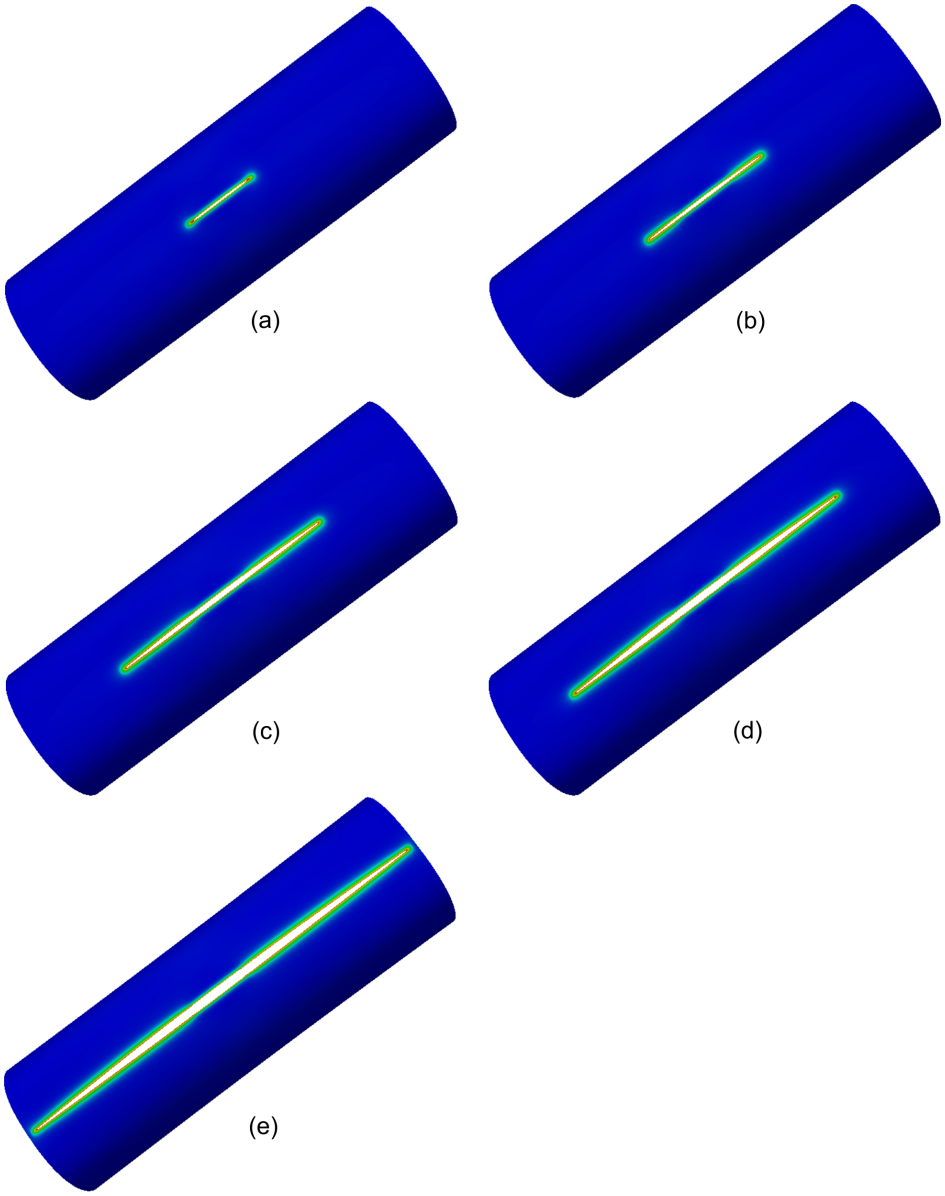

Figure 19: Notched cylinder without tear straps under internal pressure. Crack phase field at various fracture stages.

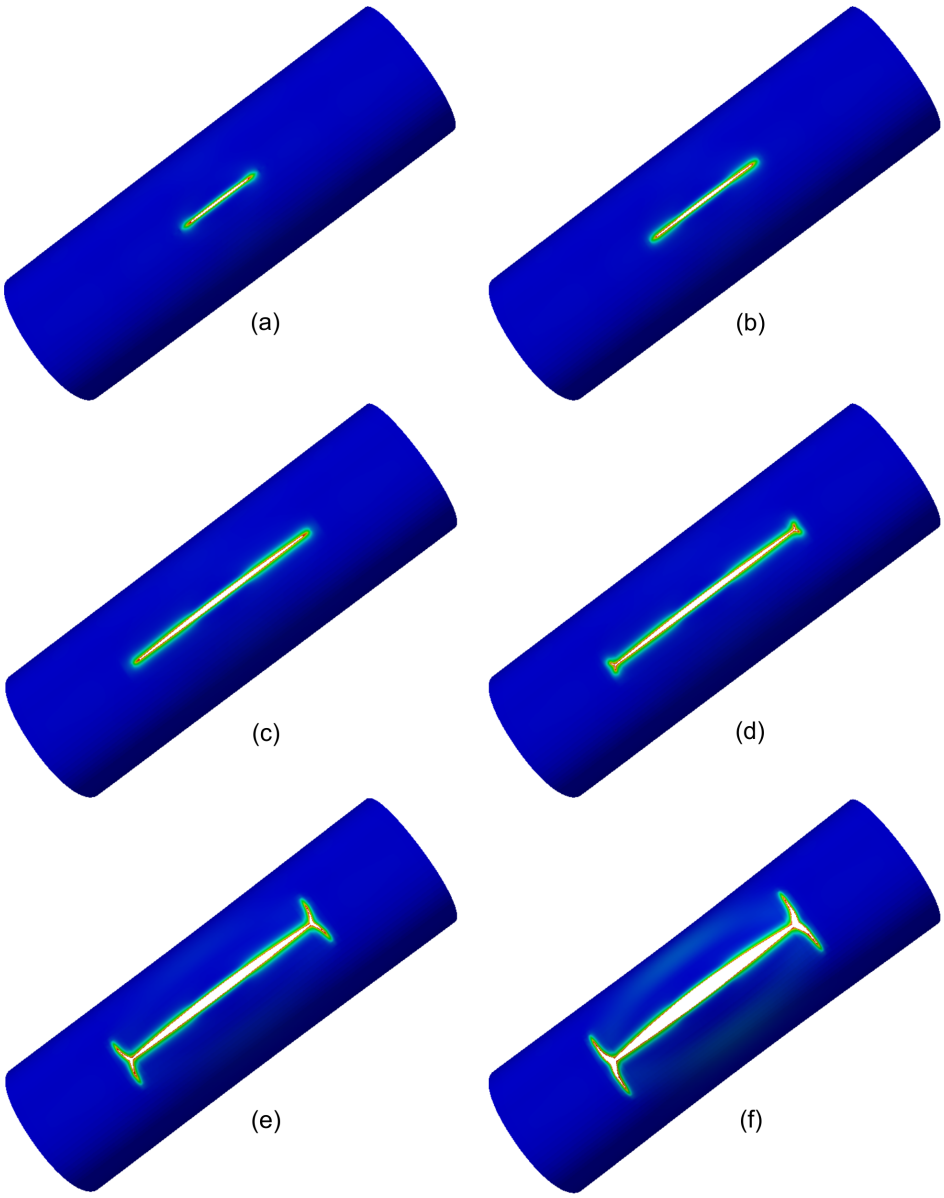

Figure 20: Notched cylinder with tear straps under internal pressure. Crack phase field at various fracture stages.

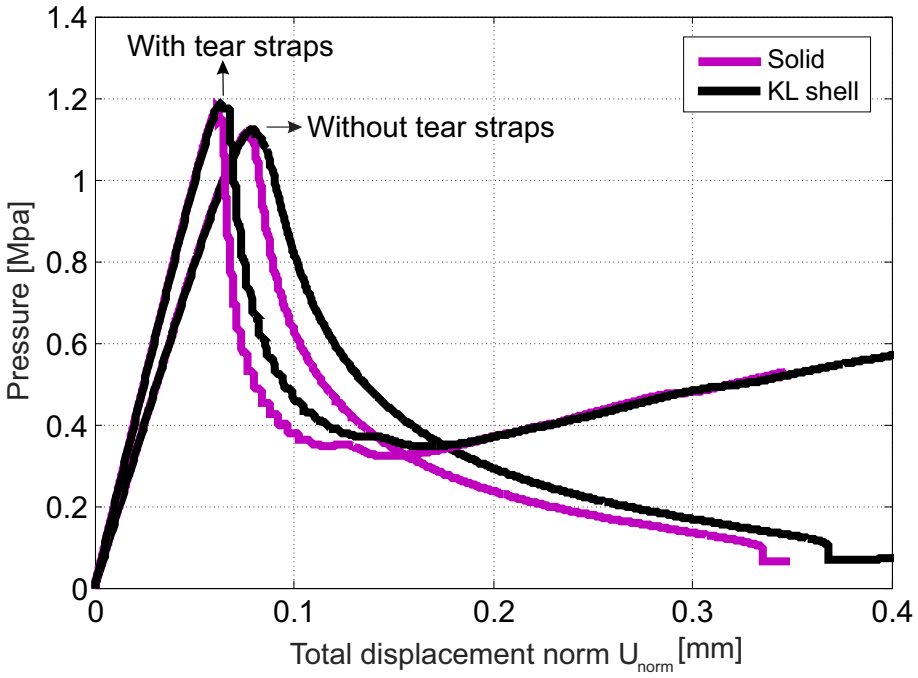

Figure 21: Notched cylinders under internal pressure. Load-displacement curves.

4. Conclusion

We presented an approach to apply phase-field modeling of fracture to thin structures like plates and shells. A focus hereby is on the correct description of fracture driven by tensile strains, within a framework where both the structure and the phase field are described as surface models, avoiding the necessity for three-dimensional discretizations or for multiple phase fields. This is a challenge for problems involving bending since the related kinematic variable (curvature or curvature change) describes a deformation which induces both tension and compression, distributed over the thickness of the structure. We showed that the spectral decomposition for the tension-compression split has to be performed on the total strain, which varies over the thickness, not on the typical shell kinematic variables related to the midsurface. As a result of this approach, the degradation of the elastic properties can vary over the thickness although the degradation function itself (being a function of the phase field) is assumed constant. This, in turn, allows for the correct degradation of the tensile parts of the stresses and strain energy, which is essential for a correct prediction of fracture. At the same time, this approach accounts for the interaction of bending and membrane strains, which is especially important in cases where compressive membrane strains reduce (or even eliminate) the tensile strains induced by bending. We have shown the applicability of the approach in several numerical examples of plate and shell structures. Detailed comparisons with results obtained by 3D solid computations, as well as with results from the literature, confirm the correctness of the method, while the numerical costs are significantly reduced compared to the solid computations. At the same time, we have also performed comparisons to a simpler model, where the tension-compression split is performed only on the membrane strains but not on the bending part. Although the results look qualitatively similar in some examples, significant quantitative differences are observed in the load-displacement curves. These comparisons demonstrate the importance of the aspects discussed above. In our opinion, the proposed approach exhibits a good combination of accuracy and efficiency for phase-field modeling of fracture in thin structures. As future work, we want to extend it to nonlinear analysis including large deformation and large strains, and ductile fracture.

Acknowledgements

TBD

Appendix A. Linearized strain variables

The definitions of $\boldsymbol{\varepsilon}^m$ and $\boldsymbol{\kappa}$ given in (20)-(21) are based on geometric quantities in the deformed and undeformed configurations, and, thus, are naturally nonlinear strain measures. For linear analysis, we can use the following linearized versions, expressed in terms of the displacement $\mathbf{u}$ and geometric variables of the undeformed configuration, indicated by $\mathring{(\cdot)}$:

$$\varepsilon^{m,L}_{\alpha\beta} = \frac{1}{2}(\mathring{\mathbf{a}}_\beta \cdot \mathbf{u}_{,\alpha} + \mathring{\mathbf{a}}_\alpha \cdot \mathbf{u}_{,\beta}) \tag{A.1}$$

$$\kappa^L_{\alpha\beta} = \\ -\mathring{\mathbf{a}}_3 \cdot \mathbf{u}_{,\alpha\beta} + \frac{1}{|\mathring{\mathbf{a}}_1 \times \mathring{\mathbf{a}}_2|}\left((\mathring{\mathbf{r}}_{,\alpha\beta} \times \mathring{\mathbf{a}}_2) \cdot \mathbf{u}_{,1} + (\mathring{\mathbf{a}}_1 \times \mathring{\mathbf{r}}_{,\alpha\beta}) \cdot \mathbf{u}_{,2} + \mathring{\mathbf{r}}_{,\alpha\beta} \cdot \mathring{\mathbf{a}}_3 \left((\mathring{\mathbf{a}}_2 \times \mathring{\mathbf{a}}_3) \cdot \mathbf{u}_{,1} + (\mathring{\mathbf{a}}_3 \times \mathring{\mathbf{a}}_1) \cdot \mathbf{u}_{,2}\right)\right) \tag{A.2}$$

where $|\cdot|$ indicates the length of a vector.

References

[1] J. Dolbow, Moës N., and Belytschko T. Modeling fracture in Mindlin-Reissner plates with the extended finite element method. *International Journal of Solids and Structures*, 37:7161–7183, 1999.

[2] P.M.A. Areias and T. Belytschko. Non-linear analysis of shells with arbitrary evolving cracks using XFEM. *International Journal for Numerical Methods in Engineering*, 195:5343–5360, 2005.

[3] R. Larsson, J. Mediavilla, and M. Fagerström. Dynamic fracture modeling in shell structures based on XFEM. *International Journal for Numerical Methods in Engineering*, 86:499–527, 2011.

[4] N. Nguyen-Thanh, N. Valizadeh, M.N. Nguyen, H. Nguyen-Xuan, X. Zhuang, P. Areias, G. Zi, Y. Bazilevs, L. De Lorenzis, and T. Rabczuk. An extended isogeometric thin shell analysis based on Kirchhoff–Love theory. *Computer Methods in Applied Mechanics and Engineering*, 284:265–291, 2015.

[5] B. Bourdin, G.A. Francfort, and J.J. Marigo. Numerical experiments in revisited brittle fracture. *Journal of the Mechanics and Physics of Solids*, 48:797–826, 2000.

[6] B. Bourdin, G.A. Francfort, and J.J. Marigo. The variational approach to fracture. *Journal of Elasticity*, 91:5–148, 2008.

[7] G.A. Francfort and J.J. Marigo. Revisiting brittle fractures as an energy minimization problem. *Journal of the Mechanics and Physics of Solids*, 46:1319–1342, 1998.

[8] H. Amor, J.J. Marigo, and C. Maurini. Regularized formulation of the variational brittle fracture with unilateral contact: Numerical experiments. *Journal of the Mechanics and Physics of Solids*, 57:1209–1229, 2009.

[9] C. Kuhn and R. Müller. A continuum phase field model for fracture. *Engineering Fracture Mechanics*, 77:3625–3634, 2010.

[10] C. Miehe, M. Hofacker, and F. Welschinger. A phase field model for rate-independent crack propagation: robust algorithmic implementation based on operator splits. *Computer Methods in Applied Mechanics and Engineering*, 199:2765–2778, 2010.

[11] M.J. Borden, C.V. Verhoosel, M.A. Scott, T.J.R. Hughes, and C.M. Landis. A phase-field description of dynamic brittle fracture. *Computer Methods in Applied Mechanics and Engineering*, 217-220:77–95, 2012.

[12] T. Gerasimov and L. De Lorenzis. A line search assisted monolithic approach for phase-field computing of brittle fracture. *Computer Methods in Applied Mechanics and Engineering*, 2016.

[13] M. Ambati, T. Gerasimov, and L. De Lorenzis. A review on phase-field models of brittle fracture and a new fast hybrid formulation. *Computational Mechanics*, 55:383–405, 2014.

[14] F.P. Duda, A. Ciarbonetti, P.J. Sanchez, and A.E. Huespe. A phase-field/gradient damage model for brittle fracture in elastic-plastic solids. *Computational Mechanics*, 65:269–296, 2014.

[15] M.J. Borden. *Isogeometric analysis of phase-field models for dynamic brittle and ductile fracture*. PhD thesis, University of Texas at Austin, 2012.

[16] C. Miehe, M. Hofacker, L. Schänzel, and F. Aldakheel. Phase field modeling of fracture in multi-physics problems. Part II. Coupled brittle-to-ductile failure criteria and crack propagation in thermo-elastic-plastic solids. *Computer Methods in Applied Mechanics and Engineering*, 294:486–522, 2014.

[17] M. Ambati, T. Gerasimov, and L. De Lorenzis. Phase-field modeling of ductile fracture. *Computational Mechanics*, 55:1017–1040, 2015.

[18] R. Alessi, J.J. Marigo, and S. Vidoli. Gradient damage models coupled with plasticity: variational formulation and main properties. *Mechanics of Materials*, 80:351–367, 2015.

[19] D. Wick, T. Wick, R.J. Hellmig, and H.J. Christ. Numerical simulations of crack propagation in screws with phase-field modeling. *Computational Materials Science*, 109:367–379, 2015.

[20] M. Ambati, R. Kruse, and L. De Lorenzis. A phase-field model for ductile fracture at finite strains and its experimental verification. *Computational Mechanics*, 57:149–167, 2016.

[21] M.J. Borden, T.J.R. Hughes, C.M. Landis, A. Anvari, and I.J. Lee. A phase-field formulation for fracture in ductile materials: Finite deformation balance law derivation, plastic degradation, and stress triaxiality effects. ICES Report 16-15, University of Texas at Austin, 2016.

[22] H. Ulmer, M. Hofacker, and C. Miehe. Phase field modeling of fracture in plates and shells. *Proceedings in Applied Mathematics and Mechanics*, 12:171–172, 2012.

[23] F. Amiri, D. Millan, Y. Shen, T. Rabczuk, and M. Arroyo. Phase-field modeling of fracture in linear thin shells. *Theoretical and Applied Fracture Mechanics*, 69:102–109, 2014.

[24] P. Areias, T. Rabczuk, and M.A. Msekh. Phase-field analysis of finite-strain plates and shells including element subdivision. *Computer Methods in Applied Mechanics and Engineering*, 2016.

[25] M. Ambati and L. De Lorenzis. Phase-field modeling of brittle and ductile fracture in shells with isogeometric NURBS-based solid-shell elements. *Computer Methods in Applied Mechanics and Engineering*, 2016.

[26] T.J.R. Hughes, J.A. Cottrell, and Y. Bazilevs. Isogeometric analysis: CAD, finite elements, NURBS, exact geometry, and mesh refinement. *Computer Methods in Applied Mechanics and Engineering*, 194:4135–4195, 2005.

[27] J. Kiendl, K.-U. Bletzinger, J. Linhard, and R. Wüchner. Isogeometric shell analysis with Kirchhoff-Love elements. *Computer Methods in Applied Mechanics and Engineering*, 198:3902–3914, 2009.

[28] J. Kiendl, Y. Bazilevs, M.-C. Hsu, R. Wüchner, and K.-U. Bletzinger. The bending strip method for isogeometric analysis of Kirchhoff-Love shell structures comprised of multiple patches. *Computer Methods in Applied Mechanics and Engineering*, 199:2403–2416, 2010.

[29] N. Nguyen-Thanh, J. Kiendl, H. Nguyen-Xuan, R. Wüchner, K. U. Bletzinger, Y. Bazilevs, and T. Rabczuk. Rotation free isogeometric thin shell analysis using PHT-splines. *Computer Methods in Applied Mechanics and Engineering*, 200(47-48):3410–3424, 2011.

[30] D. J. Benson, Y. Bazilevs, M.-C. Hsu, and T. J. R. Hughes. A large deformation, rotation-free, isogeometric shell. *Computer Methods in Applied Mechanics and Engineering*, 200:1367 – 1378, 2011.

[31] J. Kiendl, M.-C. Hsu, M.C.H. Wu, and A. Reali. Isogeometric Kirchhoff-Love shell formulations for general hyperelastic materials. *Computer Methods in Applied Mechanics and Engineering*, 291:280–303, 2015.

[32] A.B. Tepole, H. Kabaria, K.-U. Bletzinger, and E. Kuhl. Isogeometric Kirchhoff-Love shell formulations for biological materials. *Computer Methods in Applied Mechanics and Engineering*, 293:328–347, 2015.

[33] T.D. Duong, F. Roohbakhshan, and R.A. Sauer. A new rotation-free isogeometric thin shell formulation and a corresponding continuity constraint for patch boundaries. *Computer Methods in Applied Mechanics and Engineering*, 2016.

[34] T.-K. Uhm and S.-K. Youn. T-spline finite element method for the analysis of shell structures. *International Journal for Numerical Methods in Engineering*, 80:507–536, 2009.

[35] D. J. Benson, Y. Bazilevs, M. C. Hsu, and T. J. R. Hughes. Isogeometric shell analysis: The Reissner-Mindlin shell. *Computer Methods in Applied Mechanics and Engineering*, 199:276 – 289, 2010.

[36] W. Dornisch, S. Klinkel, and B. Simeon. Isogeometric Reissner-Mindlin shell analysis with exactly calculated director vectors. *Computer Methods in Applied Mechanics and Engineering*, 253:491–504, 2013.

[37] W. Dornisch and S. Klinkel. Treatment of Reissner-Mindlin shells with kinks without the need for drilling rotation stabilization in an isogeometric framework. *Computer Methods in Applied Mechanics and Engineering*, 276:35–66, 2014.

[38] S. Hosseini, J.J.C. Remmers, C.V. Verhoosel, and R. de Borst. An isogeometric solid-like shell element for nonlinear analysis. *International Journal for Numerical Methods in Engineering*, 95:238–256, 2013.

[39] S. Hosseini, J.J.C. Remmers, C.V. Verhoosel, and R. de Borst. An isogeometric continuum shell element for non-linear analysis. *Computer Methods in Applied Mechanics and Engineering*, 271:1–22, 2014.

[40] R. Bouclier, T. Elguedj, and A. Combescure. Efficient isogeometric NURBS-based solid-shell elements: Mixed formulation and B-bar-method. *Computer Methods in Applied Mechanics and Engineering*, 267:86–110, December 2013.

[41] J.F. Caseiro, R.A.F. Valente, A. Reali, J. Kiendl, F. Auricchio, and R.J Alves de Sousa. On the Assumed Natural Strain method to alleviate locking in solid-shell NURBS-based finite elements. *Computational Mechanics*, 53:1341–1353, 2014.

[42] J.F. Caseiro, R.A.F. Valente, A. Reali, J. Kiendl, F. Auricchio, and R.J Alves de Sousa. Assumed Natural Strain NURBS-based solid-shell element for the analysis of large deformation elasto-plastic thin-shell structures. *Computer Methods in Applied Mechanics and Engineering*, 284:861–880, 2015.

[43] D.J. Benson, S. Hartmann, Y. Bazilevs, M.-C. Hsu, and T.J.R. Hughes. Blended isogeometric shells. *Computer Methods in Applied Mechanics and Engineering*, 255:133–146, 2013.

[44] R. Echter, B. Oesterle, and M. Bischoff. A hierarchic family of isogeometric shell finite elements. *Computer Methods in Applied Mechanics and Engineering*, 254(0):170 – 180, 2013.

[45] B. Oesterle, E. Ramm, and M. Bischoff. A shear deformable, rotation-free isogeometric shell formulation. *Computer Methods in Applied Mechanics and Engineering*, 307:235–255, 2016.

[46] M.J. Borden, T.J.R. Hughes, C.M. Landis, and C.V. Verhoosel. A higher-order phase-field model for brittle fracture: Formulation and analysis within the isogeometric analysis framework. *Computer Methods in Applied Mechanics and Engineering*, 273:100–118, 2014.

[47] C. Hesch, S. Schuss, M. Dittmann, M. Franke, and Weinberg K. Isogeometric analysis and hierarchical refinement for higher-order phase-field models. *Computer Methods in Applied Mechanics and Engineering*, 303:185–207, 2016.

[48] D. Schillinger, M.J. Borden, and H. Stolarski. Isogeometric collocation for phase-field fracture models. *Computer Methods in Applied Mechanics and Engineering*, 284:583–610, 2015.

[49] P. Areias and T. Rabczuk. Finite strain fracture of plates and shells with configurational forces and edge rotations. *International Journal of Numerical Methods in Engineering*, 94:1099–1122, 2013.

[50] P. Areias, J. Garção, E.B. Pires, and Barbosa J.I. Exact corotational shell for finite strains and fracture. *Computational Mechanics*, 48:385–406, 2011.

[51] F. Armero and D. Ehrlich. Finite element methods for the multi-scale modeling of softening hinge lines in plates at failure. *Computer Methods in Applied Mechanics and Engineering*, 195:1283–1324, 2006.

[52] A.L. Keesecker, C.G. Davila, E.R. Johnson, and J.H. Starnes. Crack path bifurcation at a tear strap in a pressurized shell. *Computers & Structures*, 81:1633–1642, 2003.

[53] M. Kosai, A. Shimamoto, C.T. Yu, A.S. Kobayashi, and P.W. Tan. Axial crack propagation and arrest in a pressurized cylinder: An experimental-numerical analysis. *Experimental Mechanics*, 39:256–264, 1999.